The SPICA-SAFARI Detector System: TES Detector Arrays With Frequency-Division Multiplexed SQUID Readout

B. D. Jackson, P. A. J. de Korte, J. van der Kuur, P. D. Mauskopf, J. Beyer, M. P. Bruijn, A. Cros, J.-R. Gao,
D. Griffin, R. den Hartog, M. Kiviranta, G. de Lange, B.-J. van Leeuwen, C. Macculi, L. Ravera, N. Trappe,
H. van Weers, and S. Withington

Abstract—The SAFARI instrument is a far-infrared imaging Fourier transform spectrometer for JAXA's SPICA mission. Taking advantage of the low emission of SPICA's 5 K telescope, SAFARI will provide sky background-limited, Nyquist-sampled spectroscopic imaging of a $2' \times 2'$ field-of-view over 34–210 μm, creating significant new possibilities for far-infrared astronomy. SAFARI's aggressive science goals drive the development of a unique detector system combining large-format Transition Edge Sensor arrays and frequency division multiplexed SQUID readout with a high $160\times$ multiplexing factor. The detectors and their cold readout electronics are packaged into 3 focal plane arrays that will be integrated into SAFARI's focal plane unit. Here we present the preliminary system design and current development status of the SAFARI detector system.

Index Terms—Astrophysics, bolometers, frequency-division multiplexing, superconducting devices, system-level design.

I. INTRODUCTION

FAR-INFRARED (far-IR) observations are critical to answering fundamental questions in astronomy [1], including the following.

— How do galaxies and stars form and evolve?
— How do protoplanetary disks evolve and how do they relate to our own Solar System?

However, far-IR observations also face major technical challenges. To start with, the atmosphere is virtually opaque in the far-IR, requiring space or stratospheric observatories. The development of these observatories is further complicated by two factors: 1) diffraction at long wavelengths requires large telescopes to obtain high angular resolution; and 2) thermal emission from a telescope warmer than ~ 5 K is orders of magnitude brighter than the weak far-IR signals of interest.

To-date, space observatories have addressed one or the other of these challenges, but not both. Small (diameter <1 m) cryogenic telescopes like ISO [2] and Spitzer [3] provided very high sensitivities, but with limited angular resolution. Similarly, while ESA's Herschel Space Observatory is revolutionizing far-IR astronomy with its 3.5-m telescope [4], its passively cooled 80-K telescope's thermal emission is $\sim 10^6$ times brighter than the far-IR sky background.

The Japanese Space Agency's proposed SPICA mission will be the first to answer both of these challenges by actively cooling a large (3.25-m) telescope to below 6 K to enable sky-background-limited observations at 4–210 μm [1]. In doing so, SPICA offers the potential for orders of magnitude higher sensitivity than is achieved in Herschel.

When considering SPICA's potential sensitivity improvements versus Herschel, one must consider photometry and spectroscopy separately. In photometry, SPIRE [5], [6] and the longest wavelength (160 μm) channel of PACS [7] are confusion-limited—longer integrations do not detect weaker sources because they are not resolved by the 3.5-m telescope. PACS' shorter wavelength (110 and 70 μm) channels are not confusion-limited, and here higher sensitivity will increase mapping speeds and enable larger-area surveys. This being said, the real far-IR niche for SPICA is in spectroscopy, as the PACS spectrometer is sensitivity-limited—while it benefits from Herschel's large telescope, it is limited to observations of relatively few and relatively strong sources, and to narrow-band spectroscopic maps. Thus, while the Herschel photometers are producing stunning large-area maps, revealing not-before-seen structure in the interstellar medium in our galaxy and resolving large numbers of extragalactic sources, the spectrometers are only touching the tip of this iceberg. The ability to make large-area spectroscopic maps over the full far-IR band will dramatically change our picture of the universe by enabling

blind, wide-field spectroscopic surveys to characterize the chemistry and dynamics of many sources. This is the next far-IR revolution that SPICA will enable, and it is this goal that drives the design of SAFARI—the SPICA Far-Infrared Instrument.

This paper summarizes the preliminary design concept for the detector system at the heart of the SAFARI instrument.

II. SAFARI INSTRUMENT CONCEPT

SAFARI is a far-IR imaging Fourier transform spectrometer (FTS), being developed by a consortium of European and Canadian institutes. An FTS concept similar to the SPIRE instrument [8] has been selected as the optimum given achievable detector sensitivities—an FTS instrument in SPICA will reach background-limited sensitivities for detector Noise Equivalent Powers (NEPs) of $\sim 2 \times 10^{-19}$ W/Hz$^{1/2}$, which should be achievable within the instrument's development timeline (for detectors operating at 50 mK). In principle, a grating spectrometer could achieve higher point-source sensitivity than an FTS, as the sky background on each detector element would be diluted by the spectrometer [9]. However, exploiting this advantage requires detectors with much higher sensitivities ($NEP_d \sim 10^{-20}$ versus 10^{-19} W/Hz$^{1/2}$)—an order of magnitude lower than the state of the art. With this in mind, and recognizing the FTS "multiplex advantage" (a single SAFARI FTS scan will produce a full-resolution spectrum over 34–210 μm, for each pixel in the instrument's $2' \times 2'$ field of view), an FTS is seen to best address the need for large-area, wide-band spectroscopic mapping. The FTS concept also allows high-sensitivity photometry without added complexity by fixing the mechanism position and scanning the telescope in an on-the-fly mapping mode. This sacrifices sensitivity, as only 50% of the incident power reaches each detector. However, with a low-background telescope and high-sensitivity detectors a factor of 100 improvement in photometric sensitivity versus PACS can still be realized.

Table I summarizes key SAFARI instrument performance requirements. These will be realized using a Mach Zender FTS with 3 detector bands. One input port of the FTS will be coupled to the telescope and the second to a flat-field calibration source. At the output of the FTS, one port will be used for the instrument's long-wavelength channel (110–210 μm) and the second for the medium- and short-wavelength channels (34–60 and 60–110 μm, split with a dichroic beamsplitter). The FTS concept builds on a mechanism developed at TNO for the Darwin mission [10], with magnetic bearings enabling high-precision, low-dissipation operation.

The SPICA cooling system will provide 4.5 and 1.7 K temperature levels, with the bulk of the instrument at 4.5 K and the final optical elements and detector housings at 1.7 K to reduce stray-light on the detectors. The SAFARI detectors require a 50 mK base temperature. This is provided by a 2-stage sorption/ADR cooler from CEA/SBT [11] that will provide 1 μW of heat-lift at 50 mK, with a 30 hour hold-time.

SAFARI's high sensitivity goals, plus operational and calibration aspects of a fast-scan FTS, result in a unique and challenging set of performance requirements for SAFARI's detectors. These are summarized in Table II. The system is further defined by extremely tight constraints from interfaces with the

TABLE I
KEY SAFARI PERFORMANCE REQUIREMENTS

Characteristic	Requirement
Wavelength range	34-210 μm
Instantaneous field of view	2'x2'
Angular resolution	Diffraction-limited for $\lambda \geq 5$ μm
Spatial sampling	Per wavelength band, Nyquist-sampled at band-center [a]
Focal plane fill factor	80% (goal)
Spectral resolution	
- photometric imaging	R ~ 2-3
- low-resolution mode	R ~ 100 @ 100 μm
- medium-resolution mode	R ~ 2000 @ 100μm
Sensitivity	
- photometric	< 50μJy (5σ-1 hr) [a]
- spectral (med. res. mode)	< few x10^{-19} W/m^2 (5σ-1 hr) [a]
Maximum signal level	
- 57-210μm	0.5Jy
- 34-57μm	10 Jy [b]

[a] The required spatial sampling may be achieved with post-processing (i.e. with a telescope dither mode) if this does not significantly degrade observing efficiency.

[b] Instrument sensitivity may be degraded (eg. by the use of neutral density filters) for input signal levels greater than 0.5 Jy.

TABLE II
KEY SAFARI DETECTOR SYSTEM PERFORMANCE REQUIREMENTS

Characteristic	Requirement
Wavelength bands	34-60, 60-110, 110-210 μm [a]
Number of pixels	61x61, 34x34, 18x18 [a,b]
Sensitivity	
- goal	2 x 10^{-19} W/Hz$^{1/2}$ [b]
- requirement	4.5, 3.6, 3.5 x 10^{-19} W/Hz$^{1/2}$ [a,b]
Focal plane geometrical filling factor (area)	80% (goal)
Coupling efficiency x filling factor	64% (goal) 56% (requirement)
Minimum system response speed	40, 28, 13 Hz [a]
Saturation power	~ 4 fW [a,b]

[a] Where 3 values are given, these apply to the system's short, medium, and long wavelength bands, in that order.

[b] The NEP goal and requirements assume a 14% instrument optical efficiency (not including detector fill factor or coupling efficiency) and Nyquist-sampled detector arrays. For filled arrays with less-than-Nyquist sampling (i.e. fewer pixels but the same field of view), NEP figures and saturation powers scale with pixel dimension and area.

SAFARI instrument and the SPICA spacecraft, with the most significant summarized in Table III.

The remainder of this paper describes the conceptual design of a detector system that complies with these requirements.

III. SAFARI DETECTOR SYSTEM

The SAFARI detector system includes three large-format detector arrays, control and readout electronics to operate these detectors (including both room-temperature and cryogenic elements), and infrastructure that is required to mount and operate the ultra-sensitive electronics in SAFARI's Focal Plane Unit.
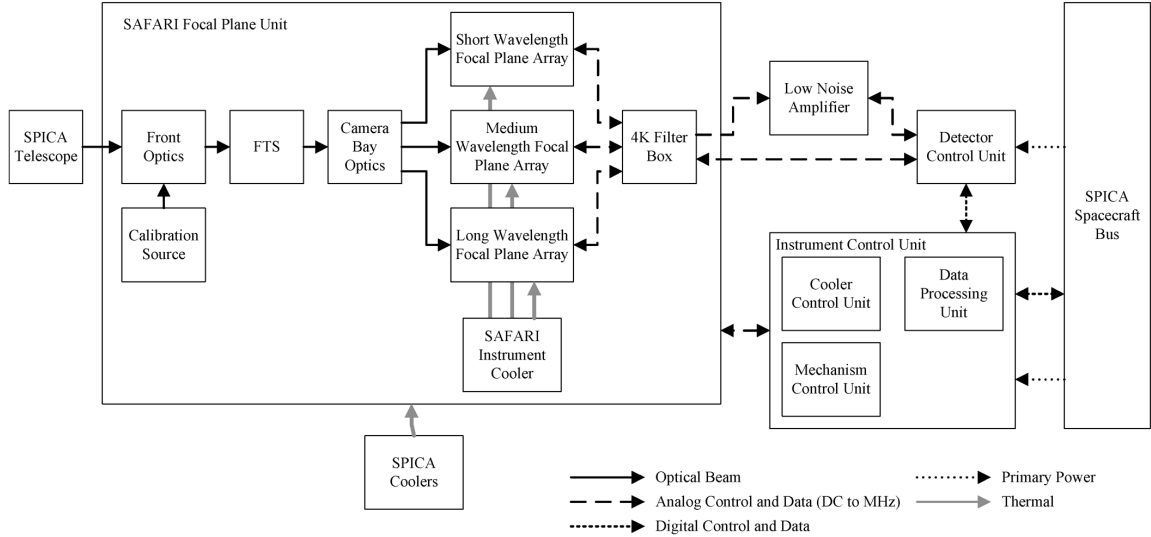
Fig. 1. Block diagram of the SAFARI instrument, focusing on the elements of the detector system (Focal Plane Array+4 K Filter Box+Low Noise Amplifier+Detector Control Unit).

TABLE III
KEY SAFARI DETECTOR SYSTEM INTERFACE CONSTRAINTS

Characteristic	Requirement
Focal plane active area	32 mm x 32 mm
Warm electronics power consumption	70 W (at primary) [a]
Thermal	
- cryo-harness passive load @ 4.5 K	2.5 mW (TBC) [a]
- 4.5 K dissipation	3 mW [a]
- 1.7 K dissipation	0.5 mW [a]
- 50 mK total heat-load	0.8 μW [a]
EMC	
- radiated E-fields	TBD V/m @ 2 & 8 GHz
- common-mode structure noise	TBD V p-p

[a] including 30% margins on heat-loads and 20% margins on power.

These elements are divided over the following units within the instrument (see Fig. 1):

— 3 "Focal Plane Arrays" (FPAs), each containing one detector array, its multiplexed SQUID amplifier readout electronics, and shielding and filtering needed to operate these components within the SPICA environment;

— a 4.5-K filter box containing the first layer of filtering for the harness leading to the detectors and cold electronics;

— an LNA operating at ~ 136 K that amplifies the weak analog output signals from the cryogenic readout electronics;

— DCU containing room-temperature control and readout electronics.

The development of this system is split into three major focus areas that are addressed in the sections that follow:

— detector arrays, including optical coupling;
— multiplexed detector readout electronics;
— focal plane arrays.

IV. DETECTOR ARRAY CONCEPT

The SAFARI detectors combine superconducting Transition Edge Sensor (TES) thermometers with horn-coupled absorbers on SiN suspension structures to realize SAFARI's unique set of requirements for very low noise, high optical coupling efficiency, and moderate saturation power [12]. Moreover, SAFARI's sampling and field of view requirements call for arrays of up to 4000 pixels, with pixel sizes of 0.48–1.6 mm.

A. Low-NEP TES Arrays

SiN-suspended TES detectors are used in sub-mm and mm-wave detectors for many ground-based telescopes [13]–[16]. However, the move to a space-based observatory with a cryogenically cooled telescope reduces the background load on the detectors by orders of magnitude. This requires a revolutionary step in detector sensitivies, moving from typical NEPs of a few $\times 10^{-17}$ W/Hz$^{1/2}$ for ground-based observatories to a goal of 2×10^{-19} W/Hz$^{1/2}$ for SAFARI.

Considering the phonon noise that limits the ideal Noise Equivalent Power (NEP) of a TES bolometer

$$\mathrm{NEP_{ph}} = \sqrt{4\gamma k_B T_c^2 G} \; (\mathrm{W}/\sqrt{\mathrm{Hz}}) \qquad (1)$$

and recognizing that γ is $\sim$0.5, two parameters can be adjusted to optimize sensitivity: T_c (the superconducting transition temperature of the TES thermometer), and G (the thermal conductivity of the link between the absorber and the thermal bath). However, T_c cannot be reduced substantially versus previous systems. ($T_b = 50$ mK is a practical limit for the cold stage temperature and T_c should be at least $2 \cdot T_b$, so $T_c = 100$ mK is baselined for SAFARI, versus 120–450 mK in previous systems.) Rather, a quantum leap in detector performance for SAFARI requires a very low thermal conductance to the thermal bath ($G \sim 0.2$ pW/K).

Extremely low conductivity thermal suspensions will be realized using very-high aspect ratio SiN structures. Indeed, for the nominal 850 μm pixel size of the instrument's mid-wavelength band, the classical diagonal leg TES suspension geometry (see Fig. 2) allows SiN leg lengths of ~ 450 μm, which calls for legs of approximately 1 μm width and 250 nm thickness to reach the
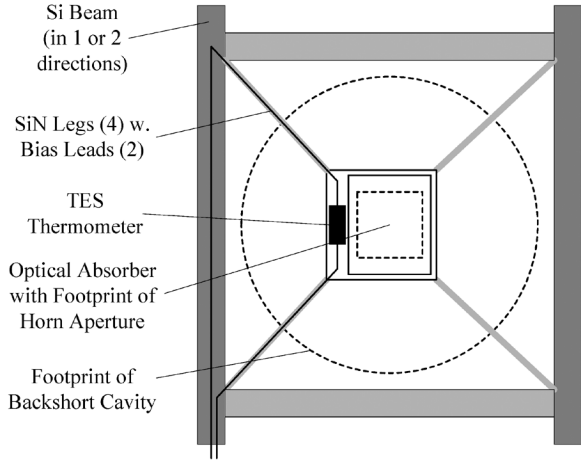
Fig. 2. Schematic of a SiN-suspended, absorber-coupled TES bolometer pixel in classical "diagonal-leg" geometry. Low NEP devices require very low thermal conductivity of the SiN suspension. See [17] for alternative low-conductivity geometries.
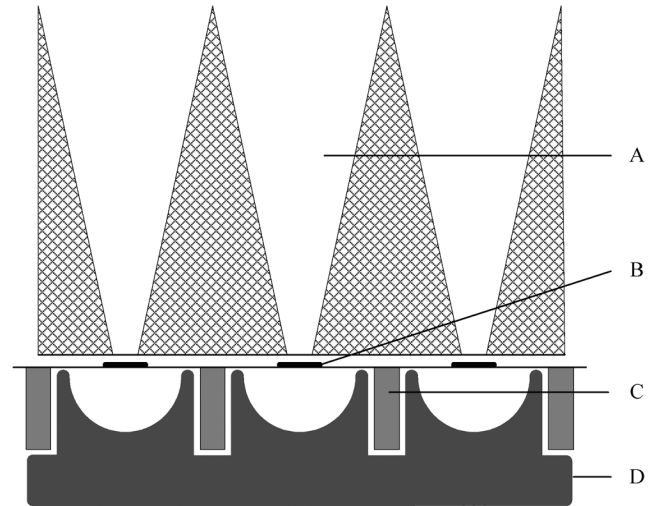

Fig. 3. SAFARI detector optical coupling geometry: A multimode pyramidal horn (A) over-illuminates a cold aperture in the instrument optics (not shown). An impedance-matched absorber on the TES island (B) fills the horn's exit aperture. Radiation that passes through the absorber is reflected back by a back-short cavity (D) that extends into the gaps between the wafer's Si beams (C). Not shown are filters in front of the horn that define the detector band-pass and provide stray light and EMI shielding.

required G. Because these are at the limits of practically realizable leg widths and thicknesses, alternative geometries are also being considered to allow very-low conductivities to be realized for the small pixels desired in the short-wavelength channel (a Nyquist-sampled array would require 480-μm pixel spacing). Reference [17] presents two alternative options being considered: a ring geometry in which the legs are wrapped up, and a parallel leg geometry in which skewed legs can be longer than the pixel spacing. At this time, the parallel leg geometry is seen as more promising, due to the large thermal mass and low stiffness of the legs in the ring-type design.

TES detector arrays for SAFARI are being developed at SRON and Cambridge. SRON is focusing on devices for the short- and medium-wavelength bands (SW and MW), using TiAu TES bilayers developed previously for X-ray microcalorimeters [18]. Cambridge is focusing on devices for the long-wavelength band (LW) using MoCu TES bilayers developed previously for mm-wave ground-based imaging arrays [19] and a new MoAu bilayer that is better suited to space qualification [20]. Both Cambridge [21] and SRON [17] typically measure detector sensitivities of $NEP_d \sim 4 - 5 \times 10^{-19}$ W/Hz$^{1/2}$ for single-pixels and small arrays ($\leq$25 pixels) of detectors with $T_c \sim 100$ mK operating at $\sim$50 mK. This is within a factor of $\sim$2 of SAFARI's goal sensitivities. Moreover, both Cambridge and SRON typically see a factor of ~ 1.5 to 3 difference between the measured detector NEP and the phonon NEP predicted from (1), bilayer T_c's, measured SiN thermal conductivities, and device geometries.

Ongoing work aims to scale to larger arrays, address the difference between the measured system noise and theoretical phonon noise, develop smaller-pitch devices for the SW band, and optimize the detector speeds. (Both Cambridge and SRON devices currently meet the detector speed goals but this needs to be monitored as detector performance is optimized.) Addressing the noise issue should also improve the devices' saturation powers, as the saturation power of a TES detector scales roughly with G, and thus with the square of NEP (for

a constant T_c and T_{bath}). Recovering a factor of 40% in the "missing" NEP could thus improve the saturation power by a factor of 2. This is significant, as the theoretical saturation power for a TES with $NEP_{\text{ph}} = 2 \times 10^{-19}$ W/Hz$^{1/2}$ is ~ 4 fW (so the devices are extremely sensitive to loading by stray-light, EMI pickup, etc.) and this 4 fW saturation power is very close to that required for SAFARI to observe 0.5 Jy "strong" sources(the design is marginal with respect to this goal).

B. Horn-coupled absorbers

The second critical aspect of the detector array design is the absorption efficiency for incoming photons. The baseline optical coupling design for SAFARI uses an impedance-matched absorber in a non-resonant cavity, with a multi-mode pyramidal horn concentrating incoming light into the cavity (see Fig. 3). This non-resonant design should offer high coupling efficiency over SAFARI's nearly octave-wide detector bands.

A multi-mode horn is used to realize efficient coupling to a cold (1.7 K) aperture stop in the instrument, where the stop is an undersized image of the telescope secondary mirror. The horn over-illuminates this stop to maximize the coupling efficiency for incoming photons, with the spillover terminated at 1.7 K to minimize the background load on the detectors. The pyramidal horn geometry lends itself to fabrication of large arrays by a process of wire-cutting of aluminum mandrels, electroforming of copper, and dissolution of the aluminum to produce the final horns [22]. The input apertures of the horns are defined by the required detector pitch (nominally 1.6, 0.85, and 0.48 mm for Nyquist sampling of an F/20 beam in the LW, MW, and SW bands). The output apertures are nominally equal to the bands' central wavelengths (160, 85, and 48 μm) to realize multi-mode coupling while also minimizing the absorber size. The horns' aspect ratios are tuned for efficient coupling to the F/20 beam defined by the cold stop, with a baseline of a 3° half-angle.

The optical absorber on the TES pixel covers the exit aperture of the horn, with a back-short cavity located behind it. The absorber's surface impedance is defined by the impedance of the cavity (slightly higher than free space), in which case $\sim 50\%$ of the incident light is absorbed on the first pass, with the remainder passing through and into the approximately hemispherical cavity. High cavity reflectivity ensures that the majority of this radiation is reflected back to the TES pixel, with small amounts being lost through unavoidable gaps between the horn, TES pixel membrane, and the top edge of the cavity, and due to transmission back through the absorber and out the mouth of the horn. The absorber is oversized relative to the aperture of the horn ($L_{\min} \sim 1.5\lambda$) to accommodate alignment tolerances and increase the absorption efficiency. The detailed absorber and cavity geometry are subject to ongoing optimization (e.g., enlarging the absorber to increase efficiency shortens the SiN legs for a given pixel size, and thus gives a higher G and NEP).

References [23] and [24] provide details of ongoing measurements of the optical coupling efficiency of SAFARI-like SW and LW single-pixels—these preliminary measurements indicate coupling efficiencies of $\sim 50\%$, but with the horn-absorber-cavity geometry still to be optimized. Electromagnetic modeling of the horn-absorber-cavity design is also ongoing [25].

V. MULTIPLEXED DETECTOR READOUT

The SAFARI detector readout electronics include three main groups of components:
— room-temperature electronics that provide signal processing, plus bias and control for the cold electronics;
— a SQUID amplifier chain that amplifies the very weak (sub-μA) analog signals from the low-impedance TES detectors (with normal-state resistances < 100 mΩ), without degrading the system noise (~ 10 pA/Hz$^{1/2}$);
— cold multiplexing electronics that allow each SQUID amplifier to read-out many TES pixels, to minimize the cable harness complexity and heat-loads.

The description that follows summarizes the design concept for the SQUID amplifier chain, and then focuses on the multiplexing scheme that is being applied for SAFARI.

A. SQUID Amplifier Chain for SAFARI

The very small bias currents of SAFARI's TES detectors will be read-out using a low-noise amplifier chain consisting of SQUID amplifiers at 50 mK and 1.7 K [26], [27], followed by a semiconductor (SiGe) low-noise amplifier (LNA) at 136 K [28]. The first-stage 50 mK SQUID amplifier provides low-noise amplification of the low-impedance TES bias current, with a low-impedance connection between the TES's and the SQUID ($\sim$3 nH common inductance is allowed). Because the first-stage SQUID gain is limited by an allowed dissipation of 5–10 nW per amplifier, a second-stage array SQUID amplifier at 1.7 K is needed to boost the signal power. Finally, a semiconductor amplifier at 136 K overcomes losses in the long SPICA cable harness ($\sim$15 m between the focal plane unit and warm electronics), and reduces the system's susceptibility to interference from "common mode structure noise" in the 0.05–50 MHz

range. The LNA's 136 K operating temperature is as low as feasible, given their dissipation (a few milliwatts (mW) per channel) and the spacecraft's thermal budget.

Ongoing work continues to evaluate the susceptibility of this amplifier chain to common-mode voltages, to maximize the output from the SQUID amplifiers, and to develop and optimize the SQUIDs and LNA.

B. Frequency Division Multiplexing (FDM) With Baseband Feedback (BBFB)

One of the biggest challenges facing SAFARI is the readout of up to 6000 TES detectors within the power and thermal constraints of the SPICA spacecraft noted in Table III. In particular, the very low ($\sim$2.5 mW) conductive heat-load allowed in the cable harness between the spacecraft's 30 and 4.5 K thermal shields calls for very high multiplexing ratios (i.e., maximizing the number of pixels that can be read out per SQUID amplifier chain).

SQUID amplifier multiplexing for TES detector readout generally makes use of one of two concepts:
— Time division multiplexing (TDM), in which an array of detectors is read-out sequentially by connecting each pixel to a first SQUID stage that acts as an on/off switch. The signals of these 1st stage switches are fed to common second and third stage SQUIDs for further amplification. When the switching bandwidth of the 1st stage is fast enough, this allows many TES's to be sampled within the instrument's sampling time.
— Frequency-division multiplexing (FDM), in which an array of detectors is read out in parallel by applying AC bias signals with slightly different frequencies to each detector, such that these signals can be summed and transported simultaneously in a single twisted-pair.

For both types of readout, the multiplexing factors that have been realized in systems for ground-based instrumentation are limited (e.g., 40$\times$ for the TDM system in SCUBA-II [13] and 8$\times$ for the FDM system on the ACT and SPT [29], [30]). SAFARI thus requires a significant step in multiplexing—reading out 6000 pixels with a potentially realizable 40 channels requires a multiplexing factor of 160.

Based on past developments for IXO [31], an FDM system with a multiplexing factor of 160 is baselined for SAFARI (see Fig. 4 for a block diagram). Key elements are as follows.

1) Detector AC Bias and Readout: At the core of FDM readout is the use of AC bias to operate the TES detector, in place of the DC bias typically used for single-pixel lab experiments and for TDM readout. In AC readout, the AC bias signal heats the TES into its superconducting transition, with $R \sim 0.3R_{\rm N}$. Given the MHz bias frequencies and $\sim$100 Hz detector speeds used in SAFARI a stable bias point, as can be achieved with DC bias, is possible. As for DC bias, electro-thermal feedback in the TES causes the amplitude of the resulting AC bias current to be a measure of the absorbed optical power—as power is absorbed, the bias current drops so that the TES' operating temperature remains unchanged. The result is an amplitude-modulated AC bias current that can be read-out with a SQUID amplifier and then de-modulated in warm electronics to recover the amplitude of the incident optical signal.

For SAFARI, the AC bias signals are generated in high-speed digital electronics, with reconstruction filters to create a clean analog signal and additional filtering to avoid that the detectors are saturated by noise or out-of-band signals. The demodulation and recovery of the baseband (optical) modulation also takes place in high-speed digital electronics.

2) Multiplexing: AC Bias Comb and Bias and Summing Topology: Once AC bias of a single detector is realized, the next step is to multiplex many pixels in a single SQUID channel. In its simplest form, this requires four functions: generation of a comb of AC bias carriers, distribution and separation of this comb so that each pixel sees a single carrier, recombination (summing) of the output signals from each pixel into a comb of modulated AC carriers which can be fed into a single SQUID amplifier, and eventual demodulation of the AC carriers to recover the optical modulation of each pixel.

The first and last steps are performed in warm electronics, using the processing power of high-speed digital electronics to first generate a comb of AC bias signals with settable frequencies, amplitudes, and phases, and to finally de-modulate the output comb of modulated carriers.

For multiplexed TES biasing one can select either row or column configurations. Considering a hypothetical 2-D array of pixels in which each column is connected to one SQUID amplifier chain, a row configuration implies that each pixel in a row is biased by the same frequency. This reduces the power required for AC bias generation (because the same set of carriers can be re-used for each channel), but requires extremely precise fabrication of the LC filters that separate the carriers at the input to the detector chip (because the LC filter resonance frequencies for a given row must be equal to within a fraction of the LC filter line-width, which is 200 Hz for $Q = 10\,000$ at 2 MHz). Because this is not achievable in the LC-filter production process, column biasing is used, with unique multi-frequency AC bias combsfor each readout channel (tuned to the as-measured resonances of the LC filter chips).

The modulated AC bias currents are added (summed) by means of current summing in a coil at the input of the 1st stage SQUID amplifier. (This coil is physically located on the LC filter chip, to reduce the number of interconnections between the LC filter and SQUID amplifier chips).

3) LC Filters: A key element of FDM readout is the LC-filters (one for each pixel) that: 1) separate the AC-bias comb over the individual single-bias-frequency pixels; 2) enable low-impedance voltage bias of each TES at the central frequency of its LC-filter; and 3) suppress the out-of-band Johnson noise from the pixel in each read-out chain;.

Interpixel crosstalk $(< 10^{-3})$ and baseband feedback gain-bandwidth $(>1$ kHz) requirements drive the carrier spacing (12.5 kHz) and relative accuracy (1 kHz) for these filters. This enables 160 channels in 1–3 MHz, which is a compromise between capacitor size in the LC-filters at lower frequencies, and power consumption and SQUID backaction noise at higher frequencies. The filters must also be low-loss to minimize their in-band parasitic impedances and thus ensure voltage bias of the detectors—a goal of $Q = 10\,000$ corresponds to a bandwidth of 200 Hz at 2 MHz. Finally, with up to four 160-pixel channels per LC filter chip, many components are integrated in each chip, stressing process yields, especially

for the capacitors used in the filters and the voltage dividers in the detectors' AC bias network.

A key to developing these high-Q LC filters has been the application of low-loss a: Si-h layers as the capacitor dielectric [32], [33]. This, combined with optimization of the device process to minimize step coverage issues has allowed the required Q-factors to be demonstrated in 18-pixel arrays with good yield. Fig. 5 shows the transmission spectrum of one such filter. The next step in this development is to scale to larger arrays to better quantify and further optimize the resonance frequency control and process yield.

4) Achievable Multiplexing Factor and Baseband Feedback: The achievable multiplexing ratio in this scheme can be limited by several factors, including: the bandwidth available for AC carriers, the density and accuracy with which LC filter resonances can be packed within this bandwidth, the dynamic range of the DAC's that generate the AC bias and feedback signals, and the dynamic range of the SQUID amplifiers. The SAFARI LC filter technology should allow 160 bolometer pixels to be multiplexed within a 1–3 MHz carrier band. For x-ray pulse readout [31], the dynamic range per pixel stresses the number of bits available in the DACs used for AC bias and feedback signal generation, limiting the system to $40x$ multiplexing. However, the dynamic range per pixel for SAFARI bolometer readout is less, and a $160\times$ multiplexing factor can be accommodated.

In "open-loop" FDM readout, the dynamic range of the SQUID amplifier limits the number of modulated carriers that can be combined before SQUID non-linearity degrades performance. The classic solution to this problem is to use negative feedback to suppress the signal at the input to the SQUID. However, given the long cables in SAFARI ($\sim$15 m), it is not possible to create a stable feedback loop bridging the warm and cold electronics at MHz frequencies. Fortunately, the signal at the input to the SQUID has two primary components: the comb of AC carriers, each with a stable phase shift due to cable and electronics delays, and a low-frequency (0–100 Hz) modulation of each carrier by the optical signal. A feedback signal can thus be generated in the digital electronics by modulating a comb of phase-delayed AC carriers with the baseband signals recovered from the demodulated signal output. Because the feedback loop is closed at baseband, it is stable for even the long cables in SAFARI. The maximum achievable gain-bandwidth around each AC-carrier is $\sim \Delta f/2\pi \sim 2$ kHz, where Δf is the carrier frequency separation. Given a conservative feedback loop gain-bandwidth of 1 kHz, the input signals are suppressed by a factor of 50 at 20 Hz offset from the carriers (and more closer in). This is sufficient to allow a multiplexing factor of $160\times$ to also be realized within the dynamic range of the SQUIDs.

C. System Demonstration of FDM With TES Detectors

With the demonstration of the LC filters, a key step in verifying the SAFARI system design is to demonstrate low-noise readout of TES bolometers using FDM. A first step was taken with the integration of 18-channel LC filter chips with both x-ray and bolometer pixels in 2010. The x-ray system demonstration [31] used detectors being developed for IXO, while the bolometer system used prototype 5×5 TES and horn arrays for SAFARI mid-wavelength band (with electrical NEP's
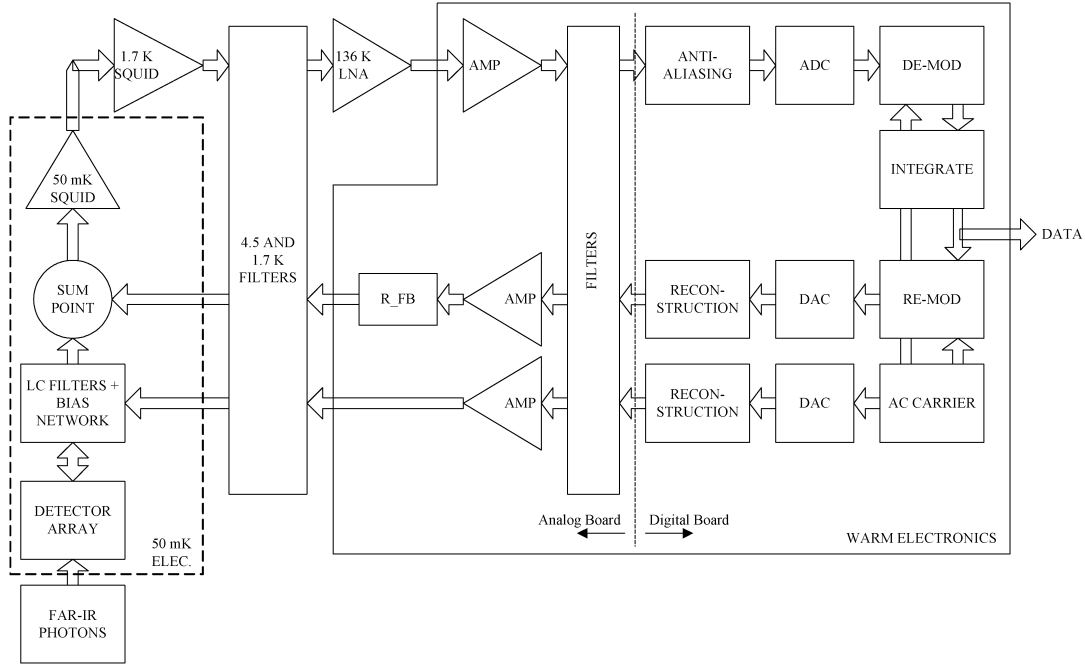
Fig. 4. Block diagram for frequency division multiplexed readout of the SAFARI TES detectors using SQUID amplifiers. Applying feedback at baseband allows the feedback loop to be closed despite (very) long cables between the cold and warm electronics, enabling a multiplexing factor of 160 pixels per SQUID channel, despite the limited dynamic range of the SQUID amplifiers.
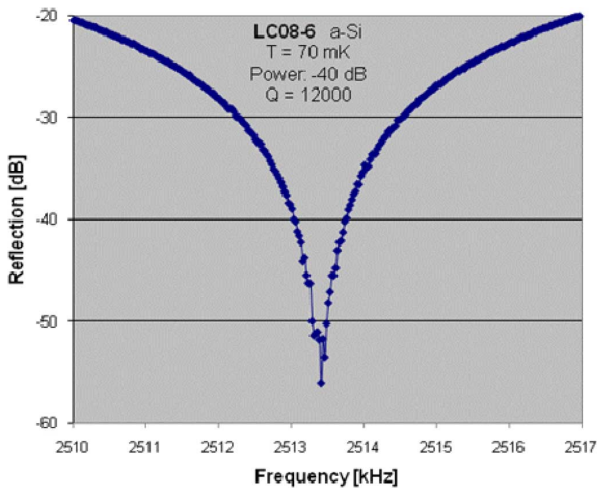

Fig. 5. Reflection spectrum of a high-Q LC filter incorporating amorphous silicon capacitors and a superconducting coil (see [32], [33]).

$\sim 2 \times 10^{-18}$ W/Hz$^{1/2}$). The x-ray tests demonstrated multiplexing of 16 pixels. Interpixel cross-talk (a critical issue for dynamic range) was low and understood, but the system noise (energy resolution in x-ray pulse readout) was higher than expected. This excess noise was traced to the particular SQUID amplifier used, and continued testing has confirmed that the required noise levels are reached with a different chip.

The next step in the FDM system demonstration is to scale-up to confirm the feasibility of larger multiplexing factors, and to demonstrate low-noise operation of bolometer arrays with FDM. For this purpose, a system containing 72-pixel LC filter and detector arrays is in production, with the detector arrays

including 64 optically coupled TES's and 8 calibration pixels. This array prototype will be used for both dark electrical measurements and optical array testing.

VI. SAFARI FOCAL PLANE ARRAY

The third major development area for the SAFARI detector system is the packaging and shielding of the ultra-sensitive detectors and cold electronics within three Focal Plane Arrays (FPAs)—one per wavelength band. Major challenges include:
— mounting and heat-sinking the large TES chips, including alignment with the horn and backshort arrays;
— high-density, low-impedance interconnections between the TES arrays and LC filter chips;
— shielding the extremely sensitive detectors and SQUIDs from straylight, high-frequency E-fields from the satellite transmitters, and low-frequency magnetic fields (including filtering of the harness and thermal straps);
— isolating the detectors and first-stage SQUIDs at 50 mK from the 1.7 K structure of the SAFARI focal plane unit;
— the complexity of the readout electronics, with 24 SQUID amplifier channels needed to readout a 4000-pixel short-wavelength array and $\sim$9 twisted pairs of wiring for each readout channel; and
— extremely tight space constraints—in one possible instrument concept, the three FPAs must fit side-by-side within the 50 cm width of the instrument, with a length (excluding magnetic baffle) of $<$10 cm.

Figs. 6 and 7 show a simplified block diagram and the preliminary design concept that addresses these issues.

Thermal Design: Each FPA contains three temperature levels (1.7 K, 300 mK, and 50 mK), separated by isostatic Kevlar suspension units. The detector array, LC filters, and 1st-stage
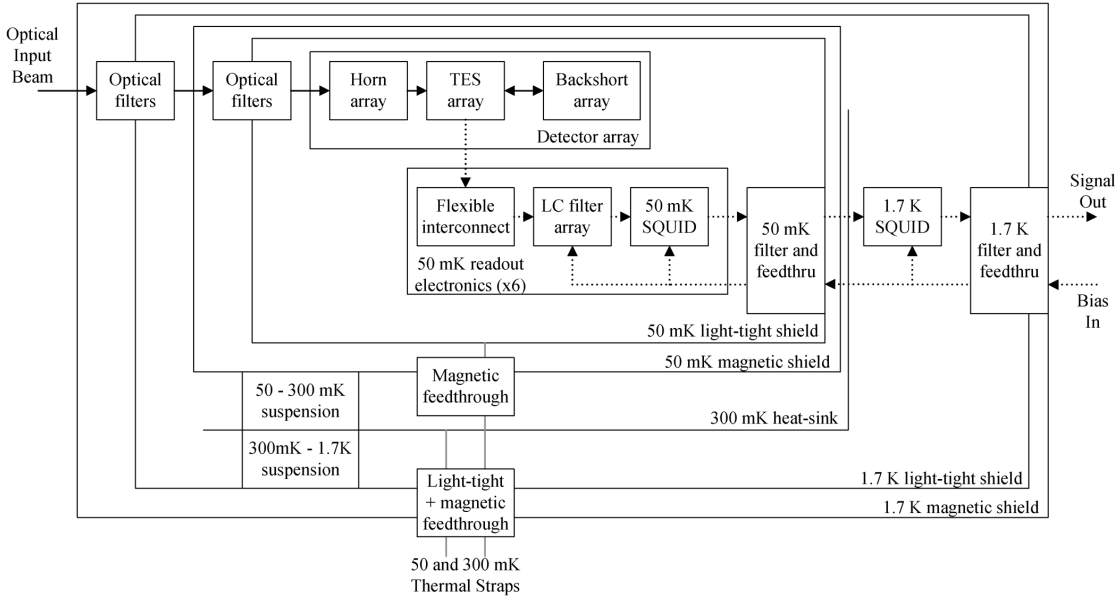
Fig. 6. SAFARI focal plane array block diagram.

SQUID amplifiers are at 50 mK, with the 2nd-stage SQUID amplifiers at 1.7 K. The 300 mK level is used as a thermal heat-sink to minimize the conductive thermal load on the 50 mK stage.

The SAFARI cooler provides up to 1 μW of cooling power at 50 mK. The total heat-load at 50 mK is dominated by the 1st-stage SQUID amplifiers, with 40 amplifiers using a few nW each. Locating the 2nd SQUID amplifier at 1.7 K helps reduce the number of wires to 50 mK and their conductive heat-loads (estimated as 5 nW/channel for 5 superconducting wire pairs + 50 nW for the Kevlar suspension of each FPA), while allowing higher dissipation in the second-stage SQUID.

Because the 300 mK stage is open, there is an extra heat-load on 50 mK from 1.7 K thermal radiation. Approximating the 50 mK stages as $10 \times 10 \times 10$ cm^3 cubes, and assuming an emissivity of 1, the total radiation load for three FPAs would be 0.1 μW. However, the emissivity of the outside of the 50 mK stage should be $\ll 1$ and absorption by the 300 mK stage will also be non-zero, so this is a conservative figure.

Shielding Design: The sensitive 50 mK components are shielded from the outside world at each of the 1.7 K and 50 mK stages. Each of these shields must suppress DC magnetic fields, radiated E-fields, and straylight; which may require double-layer shields.

The baseline design includes a cryoperm shield at 1.7 K and a Niobium shield at 50 mK. Entrance baffles maintain a high magnetic shielding efficiency, in spite of the large optical aperture (a square of 4–5 cm across). Measurements of the magnetic field susceptibility of SAFARI TES's are ongoing to verify the shielding requirements—the baseline concept is based on past tests of X-ray detectors, for which shielding to 0.1–1 nT levels was determined to be necessary [34]. The SQUID amplifiers for SAFARI will include gradiometric coils that reduce their susceptibility to magnetic fields.

A second shield at each of 1.7 K and 50 mK levels provides straylight and radiated E-field shielding. These shields are essential, as the detectors are saturated by fW's of optical or electrical loading and have post-integration noise levels of <1

aW. High-pass optical filters will close the optical apertures in each shield, providing $\sim 10^4$ attenuation for long-wavelength thermal radiation and radiated E-fields [35], [36]. Light-tight joints in the shields will be realized with meander structures coated with absorber (eg. carbon-loaded epoxy), while DC electrical feedthroughs will be realized by potting wires in a similar epoxy (after removing thick insulator layers, if necessary).

One aspect of this shielding concept that is not yet defined is EMI shielding and wiring harness filtering. E-field strengths near the SPICA optical bench are not yet known, but the satellite's transmitters (if on) will produce field strengths of >1 V/m outside the thermal shields. Such fields would couple significant power to the SAFARI detectors, and could require up to 120 dB of shielding in order to not increase the detector noise levels. While realizing such shielding will be very difficult, if not impossible, this first-order analysis highlights that the detectors are very susceptible to EMI, and that all reasonable shielding measures must be taken. With this in mind, the FPA envelope in Fig. 7 will be expanded to make room for filtering at 50 mK and 1.7 K. A third layer of filtering will also be added at the instrument's 4.5 K level.

Detector Array Mounting: Design of the mounting and heat-sinking of the detector arrays is underway. An isostatic geometry will help to ensure that the silicon TES wafer retains its lateral alignment to the copper backshort array during cooldown, with symmetrically located spring structures to absorb thermal-mechanical stresses. Separate alignment structures will simultaneously maintain the alignment of the copper horn array and backshort. Thermal contact will be realized by many wire-bonds between back-side metallization on the TES wafer and either the copper backshort or the surrounding metal structure. This heat-sinking is essential to ensure good thermalization of the TES wafer in the face of high-energy particle irradiation.

VII. Conclusion

The SAFARI detector system combines large-format TES detector arrays and frequency division multiplexed SQUID
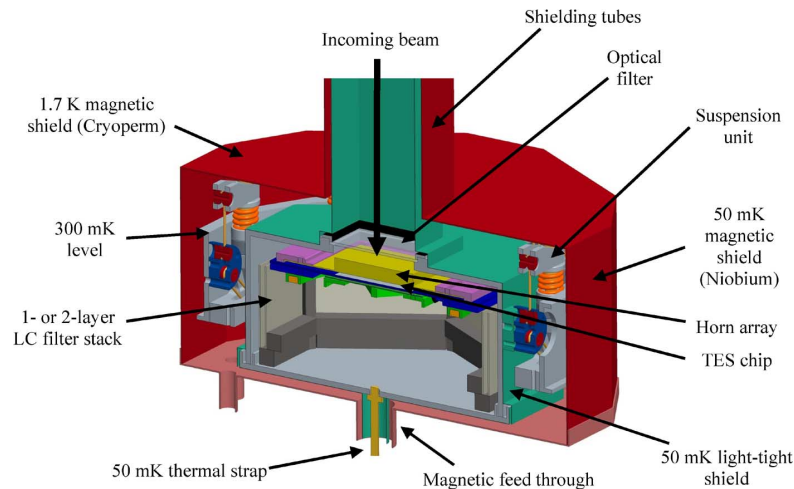
Fig. 7. Focal plane array concept. The sensitive TES arrays, LC filters, and first-stage SQUID amplifiers are located inside magnetic and light-tight shields at 50 mK, with a second layer of shielding at 1.7 K. The 300 mK stage acts only as a heat-sink for the Kevlar suspension system and electrical wiring.

readout to realize low-noise operation of up to 6000 pixels in three wavelength bands covering 34–210 μm. This system addresses both the challenging performance requirements of a background-limited FTS spectrometer behind a cryogenic telescope and SPICA's tight resource constraints.

Absorber-coupled TES thermometers on SiN membrane suspensions already offer sensitivities within a factor of 2 of the goal sensitivity of $NEP_{\mathrm{elec}} = 2 \times 10^{-19}$ W/Hz$^{1/2}$. Ongoing work aims to verify the detectors' optical coupling scheme and demonstrate the design's scalability to large arrays.

Low-noise multiplexed readout of 1000's of TES detectors within SPICA's tight thermal and power constraints is a major challenge. A frequency division multiplexing system using baseband feedback to read out 160 detectors per SQUID amplifier chain is being developed. A process has been developed to produce the high-Q LC filter arrays that this system requires and first-light system demonstrations have realized multiplexing of 10–16 pixels. A critical next step is to verify the operation and performance of this system with low-NEP TES bolometers in a 64-pixel demonstration that confirms the concept's scalability.

The third major challenge in this system design is to package and shield the sensitive detectors and cold readout electronics within three Focal Plane Arrays that isolate the 50 mK electronics from the 1.7 and 4.5 K environments of the SAFARI instrument and SPICA spacecraft. A preliminary design concept is presented, with important next steps being the development of underlying technologies, including the interconnects between the TES and LC filter wafers and the shielding and filtering that is needed to operate detectors with sub-aW noise levels within a spacecraft environment.

ACKNOWLEDGMENT

REFERENCES

[1] B. Swinyard and T. Nakagawa et al., "The space infrared telescope for cosmology and astrophics: SPICA a joint mission between JAXA and ESA," *Experimental Astronomy*, vol. 23, pp. 193–219, 2009.

[2] M. F. Kessler, J. A. Steinz, and M. E. Anderegg et al., "The Infrared Space Observatory (ISO) mission," *Astronomy & Astrophysics*, vol. 315, no. 27, 1996.

[3] M. W. Werner et al., "The Spitzer space telescope mission," *Astrophysic. J. Suppl. Series*, vol. 154, pp. 1–9, Sept. 2004.

[4] G. L. Pilbratt et al., "Herschel space observatory an ESA facility for far-infrared and submillimetre astronomy," *Astronomy & Astrophys.*, vol. 518 and 521, 2010.

[5] M. J. Griffin et al., "The Herschel-SPIRE instrument and its in-flight performance," *Astronomy & Astrophys.*, vol. 518, no. L3, 2010.

[6] H. T. Nguyen et al., "Hermes: The SPIRE confusion limit," *Astronomy and Astrophys.*, vol. 518, no. L5, 2010.

[7] A. Poglitsch et al., "The Photodetector Array Camera and Spectrometer (PACS) on the Herschel space observatory," *Astronomy & Astrophys.*, vol. 518, no. L2, 2010.

[8] B. M. Swinyard et al., "The FIRST-SPIRE spectrometer a novel imaging FTS for the sub-millimetre," in *Proc. SPIE*, Munich, Germany, March 27–31, 2000, vol. 4013.

[9] C. M. Bradford et al., "Sensitive far-IR survey spectroscopy: BLISS for SPICA," in *Proc. SPIE Millimeter and Submillimeter Detectors and Instrumentation for Astronomy I*, W. D. Duncan, W. S. Holland, S. Withington, and J. Zmuidzinas, Eds., 2008, vol. 7020, p. 70201O.

[10] T. C. van den Dool et al., "SPICA/SAFARI cryogenic magnetic bearing fourier transform spectrometer mechanism," in *Proc. Int. Conf. on Space Optics (ICSO 2010)*, Rhodes, Greece, Oct. 4–8, 2010.

[11] L. Duband et al., "SPICA/SAFARI subkelvin cryogenic chain," in *Proc. 16th Int. Cryocooler Conf. Cryocoolers 16*, Atlanta, USA, May 18–20, 2010, C.

[12] P. D. Mauskopf et al., "A TES focal plane for SPICA-SAFARI," in *Proc. 21st Int. Symp. on Space THz Technol.*, Oxford, U.K., Mar. 23–25, 2010, pp. 246–255.

[13] W. Holland et al., "SCUBA-2: A 10,000-pixel submillimeter camera for the James Clerk Maxwell Telescope," in *Proc. SPIE*, 2006, vol. 6275, p. 62751E.

[14] J. Mehl et al., "TES bolometer array for the APEX-SZ camera," *J. Low Temp. Phys.*, vol. 151, pp. 697–702, 2008.

[15] J. E. Ruhl et al., "The South Pole telescope," in *Proc. SPIE*, 2004, vol. 5498, no. 11.

[16] J. G. Staguhn et al., "Instrument performance of GISMO, a 2 millimeter TES bolometer camera used at the IRAM 30 m telescope," in *Proc. SPIE*, 2008, vol. 7020, p. 702004.

[17] P. Khosropanah et al., "Low noise transition edge sensor (TES) for the SAFARI instrument on SPICA," in *22nd Int. Symp. on Space THz Technology*, Tucson, AZ, Apr. 26–28, 2011.

[18] P. A. J. de Korte *et al.*, "EURECA: A European-Japanese micro-calorimeter array," in *Proc.SPIE*, 2006, vol. 6266, no. 1.

[19] M. D. Audley *et al.*, "Performance of a microstrip-coupled TES imaging module for CMB polarimetry," in *Proc. 21st Int. Sump. on Space THz Technol.*, 2010, p. 76.

[20] D. M. Glowack, D. J. Goldie, and S. Withington, "Comparative performance of Mo/Cu vs. Mo/Au transition edge sensors for space science application," in *Proc. 21st Int. Sump. on Space THz Technol.*, 2010, p. 273.

[21] D. J. Goldie *et al.*, "Ultra-low-noise MoCu transition edge sensors for space applications," *J. App. Phys.*, vol. 109, p. 083105, 2011.

[22] D. Griffin, 2010, Private communication.

[23] P. D. Mauskopf *et al.*, "Optical characterization at 1.5–3 THz of high sensitivity TES detectors designed for future far-infrared space missions," in *22nd Int. Symp. on Space THz Technology*, Tucson, AZ, Apr. 26–28, 2011.

[24] D. Morozov *et al.*, "Optical characterization of high sensitivity TES detectors designed for the SPICA/SAFARI 30–60 mm channel," in *22nd Int. Symp. on Space THz Technol.*, Tucson, AZ, Apr. 26–28, 2011.

[25] S. Doherty and N. Trappe *et al.*, "Modelling of horn antennas and detector cavities for the SAFARI instrument at THz frequencies," in *Proc. SPIE*, 2011, vol. 7938, p. 79380J.

[26] D. Drung *et al.*, "Novel SQUID current sensors with high linearity at high frequencies," *IEEE Trans. Appl. Supercond*, vol. 19, no. 3, pt. 1, pp. 772–777, 2009.

[27] M. Kiviranta, L. Grönberg, and H. Sipola, "Two-stage locally linearized SQUID readout for frequency domain ultiplexed calorimeter arrays," *Supercond. Sci. Technol*, vol. 24, p. 045003, 2011.

[28] G. Torrioli *et al.*, "A cryo-amplifier working in a double loop-flux locked loop scheme for SQUID readout of TES detectors," in *Proc. SPIE*, (2010), vol. 7732, p. 77324I.

[29] H. Spieler, "Frequency domain multiplexing for large scale bolometer arrays," in *Monterey Far-IR, Sub-mm and mm Detector Technology Workshop Proceedings*, J. Wolf, J. Farhoomand, and C. McCreight, Eds., 2002, pp. 243–249, NASA/CP-2003-21140 and LBNL-49993.

[30] T. M. Lanting *et al.*, "Frequency domain multiplexing for bolometer arrays," *Nuclear Inst. and Methods in Phys. Res*, vol. A 520, p. 548, 2004.

[31] R. den Hartog *et al.*, "Frequency domain multiplexed readout of TES detector arrays with baseband feedback," *IEEE Trans. Appl. Supercond*, 2011.

[32] M. P. Bruijn *et al.*, "Superconducting LC filter circuits for frequency division multiplexed readout of TES detectors," *IEEE Trans. Appl. Supercond.*, 2010.

[33] M. P. Bruijn *et al.*, "High-Q LC filters for FDM readout of cryogenic sensor arrays," in *14th Int. Workshop on Low Temperature Detectors*, Heidelberg, Germany, Aug. 1–5, 2011, submitted for publication.

[34] J. W. Herder *et al.*, M. Arnaud, S. S. Murray, and T. Takahashi, Eds., "The x-ray microcalorimeter spectrometer onboard of IXO," in *SPIE Space Telescopes and Instrum. 2010: Ultraviolet to Gamma Ray*, San Diego, CA, 2010, p. 77321H-10.

[35] P. A. R. Ade *et al.*, "A review of metal mesh filters," in *Proc. SPIE*, 2006, vol. 6275, p. 62750U.

[36] P. A. R. Ade and C. Tucker, 2011, Private communication.

B. D. Jackson, photograph and biography not available at time of publication.

P. A. J. de Korte, photograph and biography not available at time of publication.

J. van der Kuur, photograph and biography not available at time of publication.

P. D. Mauskopf, photograph and biography not available at time of publication.

J. Beyer, photograph and biography not available at time of publication.

M. P. Bruijn, photograph and biography not available at time of publication.

A. Cros, photograph and biography not available at time of publication.

J. R. Gao, photograph and biography not available at time of publication.

D. Griffin, photograph and biography not available at time of publication.

R. den Hartog, photograph and biography not available at time of publication.

M. Kiviranta, photograph and biography not available at time of publication.

G. de Lange, photograph and biography not available at time of publication.

B.-J. van Leeuwen, photograph and biography not available at time of publication.

C. Macculi, photograph and biography not available at time of publication.

L. Ravera, photograph and biography not available at time of publication.

N. Trappe, photograph and biography not available at time of publication.

H. van Weers, photograph and biography not available at time of publication.

S. Withington, photograph and biography not available at time of publication.